DOI: 10.2478/aucts-2025-0001

ACTA UNIVERSITATIS CIBINIENSIS – TECHNICAL SERIES
Vol. 77 2025

EXPERIMENTAL STUDY OF THE UNIAXIAL TENSILE TEST OF ALUMINIUM EN AW 5754 H22 ALLOY PERFORATED SPECIMENS

BUCUR Ana-Maria
Lucian Blaga University of Sibiu, Sibiu, Romania

OLEKSIK Mihaela
Lucian Blaga University of Sibiu, Sibiu, Romania

VASILCA Delia-Rebeca
Lucian Blaga University of Sibiu, Sibiu, Romania

OLEKSIK Valentin
Lucian Blaga University of Sibiu, Sibiu, Romania

Corresponding author: valentin.oleksik@ulbsibiu.ro | ORCID: 0000-0002-0582-1647

Abstract: *This paper studies, through experimental studies, the uniaxial tensile test behaviour of perforated plates. Two parameters were taken into account, the diameter of the perforation and the distance between two adjacent perforations measured between the edges of the perforation. Both parameters were varied on three levels, 2.5, 3 and 4 mm for the diameter of the perforation and 2, 3 and 4 mm for the distance between two perforations. This resulted in 9 experiments, repeated 3 times. The specimens were subjected to uniaxial tensile test under static condition using Instron 5587 tensile machine and simultaneously were subjected to measurement using digital image correlation using Zeiss Corelate. The results focused on determining maximum global tensile stress on uniaxial tensile test, global strain corresponding to maximum tensile stress also for uniaxial tensile test, local major strain, local minor strain, local thickness reduction, local shear angle, local Tresca strain and local von Mises strain.*

Key words: perforated plates, uniaxial tensile test, perforation diameter, distance between perforations

1. INTRODUCTION

Perforated plates are widely used across mechanical, civil, marine, and composite engineering applications due to their favourable balance between weight reduction, functional requirements, and structural performance. However, the introduction of holes or perforations significantly alters stress distribution, deformation patterns, and failure mechanisms, making accurate characterization of their mechanical behaviour a long-standing research topic.

One of the fundamental aspects in the analysis of perforated plates is stress concentration around holes. Recent work by You et al. [1] systematically investigated stress concentration characteristics in DC04 steel plates with finite thickness, proposing modified stress concentration coefficients to account for three-dimensional effects that are not captured by classical thin-plate assumptions. Complementary analytical efforts were presented by Lavrentev et al. [2], who derived effective elastic modulus for perforated plates with regular hole lattices, providing homogenized representations suitable for large-scale structural modelling. These studies highlight the continued need to refine classical theoretical formulations to better represent realistic geometries and boundary conditions.

Several studies have focused on the tensile response and fracture behaviour of perforated plates. Experimental and theoretical analyses by Mengsha et al. [3] demonstrated the strong influence of hole size on global deformation and fracture initiation, identifying critical geometric thresholds that govern failure modes. Similar tensile investigations were conducted on metallic plates exhibiting instability phenomena, such as wrinkling, under uniaxial loading, as reported by Tang et al. [4]. For composite materials, Wang et al. [5] examined the ultimate tensile strength of carbon/glass hybrid composite perforated plates, while Hu et al. [6] evaluated failure criteria for residual tensile strength in composite laminates containing circular holes. These works collectively emphasize that material anisotropy and hybridization further complicate the stress redistribution caused by perforations.

The presence of holes frequently interacts with crack initiation and propagation. Jing et al. [7] performed uniaxial failure tests on plates containing both circular holes and pre-existing cracks, combining experiments and numerical simulations to clarify crack evolution paths. At the modelling level, Scherer et al. [8] critically assessed anisotropic phase-field fracture models, which offer promising capabilities for simulating complex crack patterns in perforated and heterogeneous materials. Fatigue-related fracture phenomena were addressed earlier by Kinoshita et al. [9], who investigated multiple crack extension and temperature effects in perforated plates under elevated-temperature fatigue loading.

Beyond simple tensile loading, perforated plates are often subjected to shear and bending in structural applications. Chen et al. [10] conducted experimental and numerical studies on the shear resistance of perforated high-strength stainless steel plate girders, demonstrating how perforation geometry influences load-bearing capacity. In marine and offshore contexts, Saad-Eldeen and Garbatov [11] evaluated the structural capacity of perforated stiffened plates through combined experimental and numerical approaches. Moreover, Huang et al. [12] investigated the flexural performance of UHPC–concrete–ECC composite members reinforced with perforated steel plates, illustrating the beneficial role of perforations in enhancing composite action and ductility.

Perforated plates under dynamic loading have also attracted attention. Granum et al. [13] studied aluminium plates with pre-formed slits subjected to blast loading, revealing altered deformation and energy absorption mechanisms compared to solid plates. Earlier analytical studies, such as that by Munemoto and Sonoda [14], examined the dynamic strength of perforated steel plate shear connectors, contributing to the understanding of rate-dependent behaviour in perforated structural components.

The influence of perforation on manufacturing processes and experimental identification of material properties has also been addressed. Leminen et al. [15] investigated the effects of mechanical perforation on press-forming processes, showing that perforations affect both formability and final mechanical performance. On the methodological side, Lecompte et al. [16] proposed mixed numerical–experimental techniques for identifying orthotropic material parameters using biaxial tensile tests, approaches that are particularly relevant for characterizing perforated and architected plates with effective anisotropy.

Overall, existing research demonstrates significant progress in understanding the elastic, plastic, fracture, and dynamic behaviour of perforated plates across a broad range of materials and loading conditions. Nevertheless, challenges remain in developing unified predictive models that simultaneously account for finite thickness effects, complex perforation patterns, material anisotropy, and multi-axial or dynamic loading. Since the present paper represents part of the research related to the incremental forming of perforated sheets, in which the stress state is both uniaxial tension and biaxial tension (in different areas of the part, of course), we tried to observe the effect of the perforation diameter and the distance between the perforated holes both on the results obtained globally, in the uniaxial tensile test, and locally using digital image correlation.

2. MATERIALS AND METHOD

For the present study, we chose a material with low formability, an aluminium magnesium alloy, more specifically EN AW 5754 H22 with a thickness of 0.5 mm. The material data obtained, based on the uniaxial tensile test are: longitudinal elastic modulus (E) = 68550 MPa, Yield stress (Ys) = 146 MPa, maximum tensile stress (σ_{max}) 225 = MPa, strain corresponding to maximum tensile stress ($\varepsilon_{\sigma max}$) = 8.1%, maximum tensile strain (ε_{max}) = 11%, hardening exponent (n) = 0.179 and strength coefficient (K) = 412 MPa.

To conduct the research, we took all the samples parallel to the rolling direction of the sheet and made circular perforations. Each circular sample had a number of three perforations in a row. Figure 1 shows the two parameters taken into account for the experiments.

DOI: 10.2478/aucts-2025-0001
ACTA UNIVERSITATIS CIBINIENSIS – TECHNICAL SERIES
Vol. 77 2025

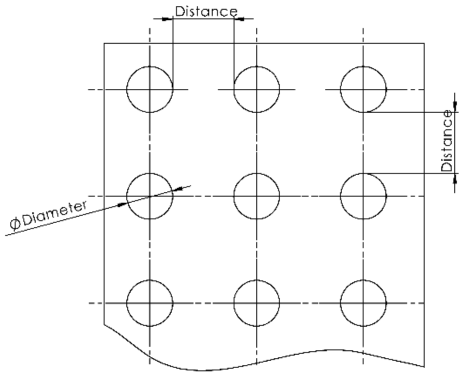

Figure 1: The parameters taken into account for uniaxial tensile test

These are the diameter of the circular perforation, called Diameter, and the distance between two perforations measured between the edges of these perforations, called Distance. Even though in the specialized literature, the pitch is most often taken into account, i.e. the distance between the centres of two successive perforations, we chose the distance between the edges so that it remains constant and is not influenced by the diameter of the perforation. Each of these two parameters was varied on three levels of variation, resulting in a 3^2 factorial experiment. All experiments were repeated three times, resulting in a total of 27 trials. Table 1 presents all 9 cases obtained for uniaxial tensile test of perforated sheets.

Table 1: The codification and the parameters for the uniaxial test of perforated sheets

Codification	Diameter [mm]	Distance [mm]
C1	2.5	2
C2	2.5	3
C3	2.5	4
C4	3	2
C5	3	3
C6	3	4
C7	4	2
C8	4	3
C9	4	4

All perforated holes were made using water jet cutting to avoid structural changes to the aluminium alloy. This was the reason why we chose the minimum perforation diameter of 2.5 mm, as water cutting technology did not allow us to achieve a smaller diameter for a thickness of 0.5 mm. A distance of 1/2 of the distance between the holes was left between the edge of the specimens and the edge of the perforated holes.

We used the Instron 5587 testing machine to conduct the tests, which has a maximum stationary load force of 300kN and an adjustable testing speed in the range of 0.001 - 500 mm/min. The specimens were vertically aligned so that the stress direction was parallel to the rolling direction. Figure 2 shows the specimen between the jaws of the Instron 5587 machine before the start of the test and immediately after the fracture occurred.

For digital image correlation we used the Aramis 12M optical measurement system together with the Zeiss Corelate software. The preparation of the specimens consisted of applying a white, matte paint to the surface of the perforated specimens and then, after they had dried, a diffusely sprayed black paint. The measurement process was preceded by calibrating the Aramis system and then by creating a surface component for each measured specimen, as seen in Figure 2, a. The acquisition rate was 5Hz for all cases.

DOI: 10.2478/aucts-2025-0001

ACTA UNIVERSITATIS CIBINIENSIS – TECHNICAL SERIES
Vol. 77 2025

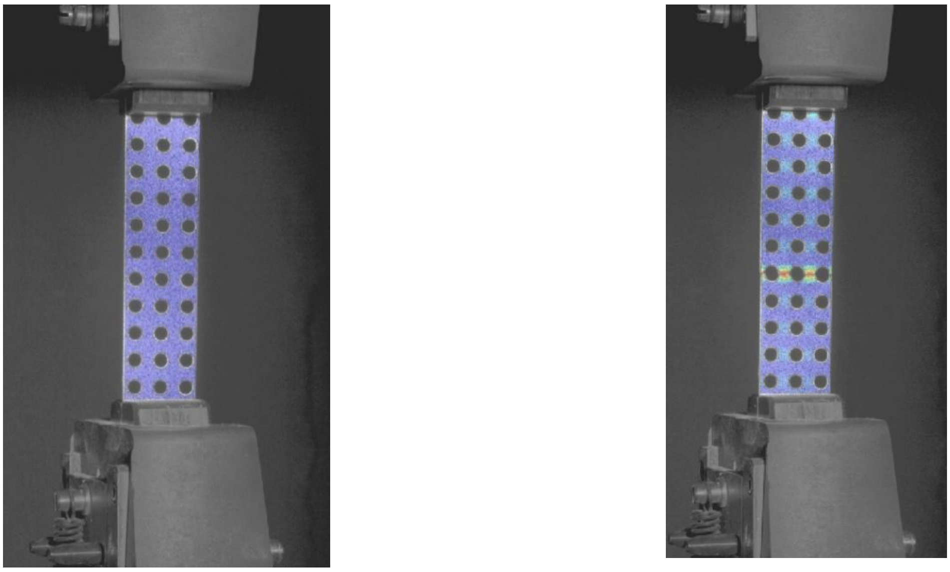

(a) **(b)**

Figure 2: The specimen clamped between the jaws of the Instron 5587 machine before the start of the test (a) and immediately after the fracture occurred (b)

3. RESULTS

The results were focused on determining maximum global tensile stress on uniaxial tensile test, global strain corresponding to maximum tensile stress also for uniaxial tensile test, local major strain, local minor strain, local thickness reduction, local shear angle, local Tresca strain and local von Mises strain. Figure 3 presents the engineering stress-engineering strain curves for the 9 analysed cases.

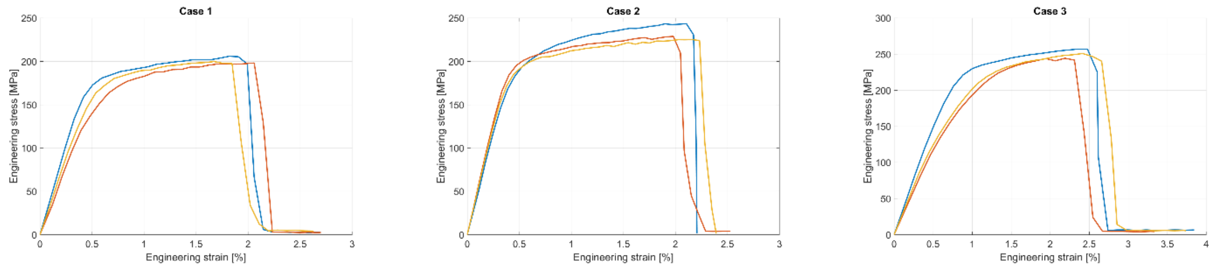

(a) **(b)** **(c)**

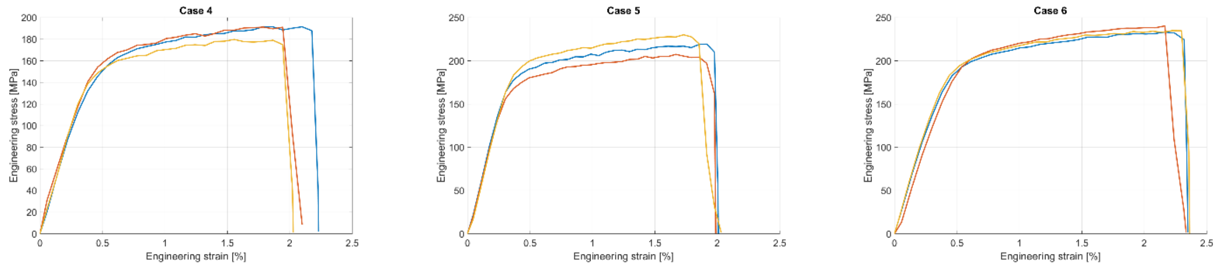

(d) **(e)** **(f)**

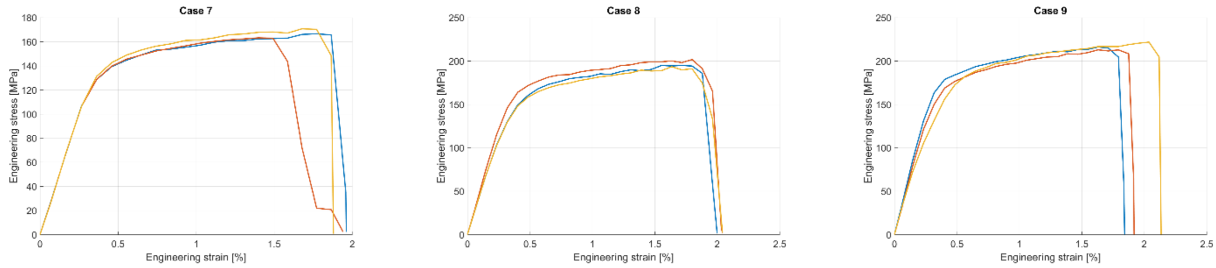

Figure 3: The engineering strain – engineering stress curves for the all nine cases (a) – C1; (b) – C2; (c) – C3;

DOI: 10.2478/aucts-2025-0001
ACTA UNIVERSITATIS CIBINIENSIS – TECHNICAL SERIES
Vol. 77 2025

(d) – C4; (e) – C5; (f) – C6; (g) – C7; (h) – C8; (i) – C9;

Table 2 presents the average values for the maximum tensile stress σ_{max} (MPa) and the Strain corresponding to maximum tensile stress $\varepsilon_{\sigma max}$ (%). The experimental data were statistically processed, using the Anderson-Darling and Grubbs tests to verify the normality hypothesis and to eliminate outliers. There were no outliers and the distribution was a normal distribution for all cases.

Table 2: The global results of the uniaxial test of perforated sheets (mean values)

Codification	Diameter [mm]	Distance [mm]	Maximum tensile stress σ_{max} [MPa]	Strain corresponding to maximum tensile stress $\varepsilon_{\sigma max}$ [%]
C1	2.5	2	201.619	1.850
C2	2.5	3	232.350	2.083
C3	2.5	4	250.574	2.320
C4	3	2	187.332	1.710
C5	3	3	218.782	1.771
C6	3	4	235.944	2.184
C7	4	2	166.750	1.617
C8	4	3	196.578	1.717
C9	4	4	216.782	1.766

Regarding the results obtained through digital image correlation, Figure 4 presents the results obtained for case C9 for: local major strain, local minor strain, local thickness reduction, local shear angle, local Tresca strain and local von Mises strain. It should be noted that all images, for all cases and specimens, were acquired at the same stage, at the stage immediately prior to the occurrence of the fracture.

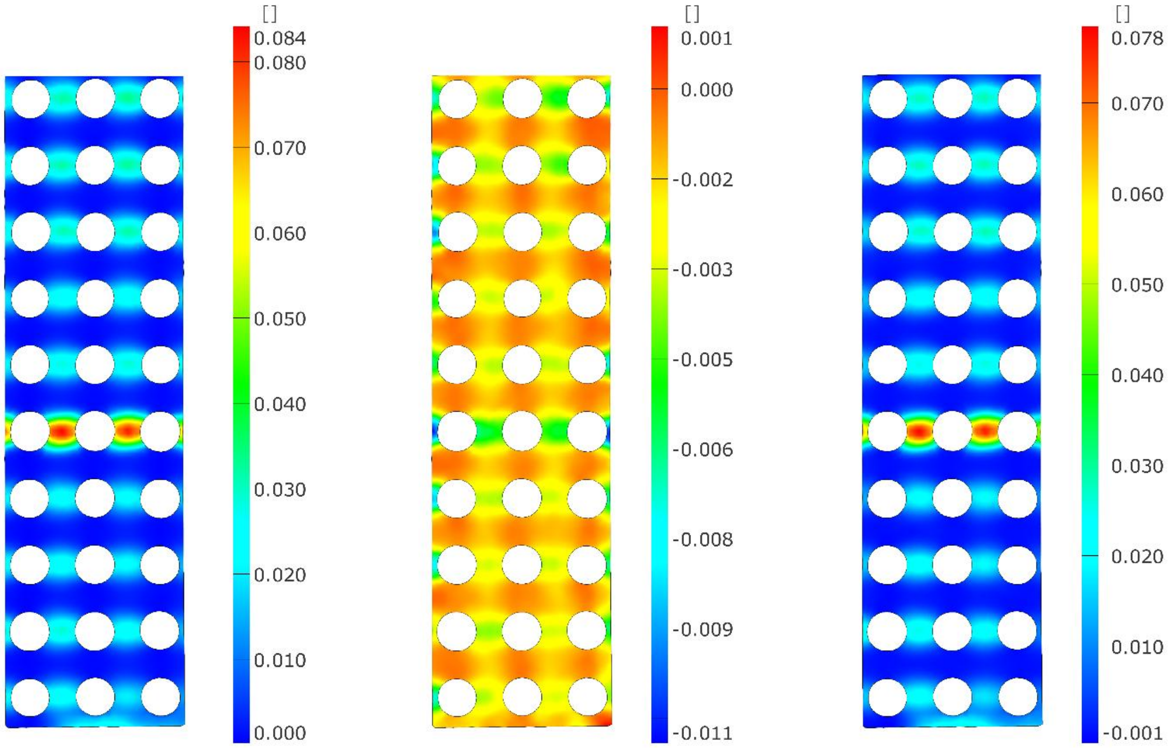

(a) **(b)** **(c)**

DOI: 10.2478/aucts-2025-0001
ACTA UNIVERSITATIS CIBINIENSIS – TECHNICAL SERIES
Vol. 77 2025

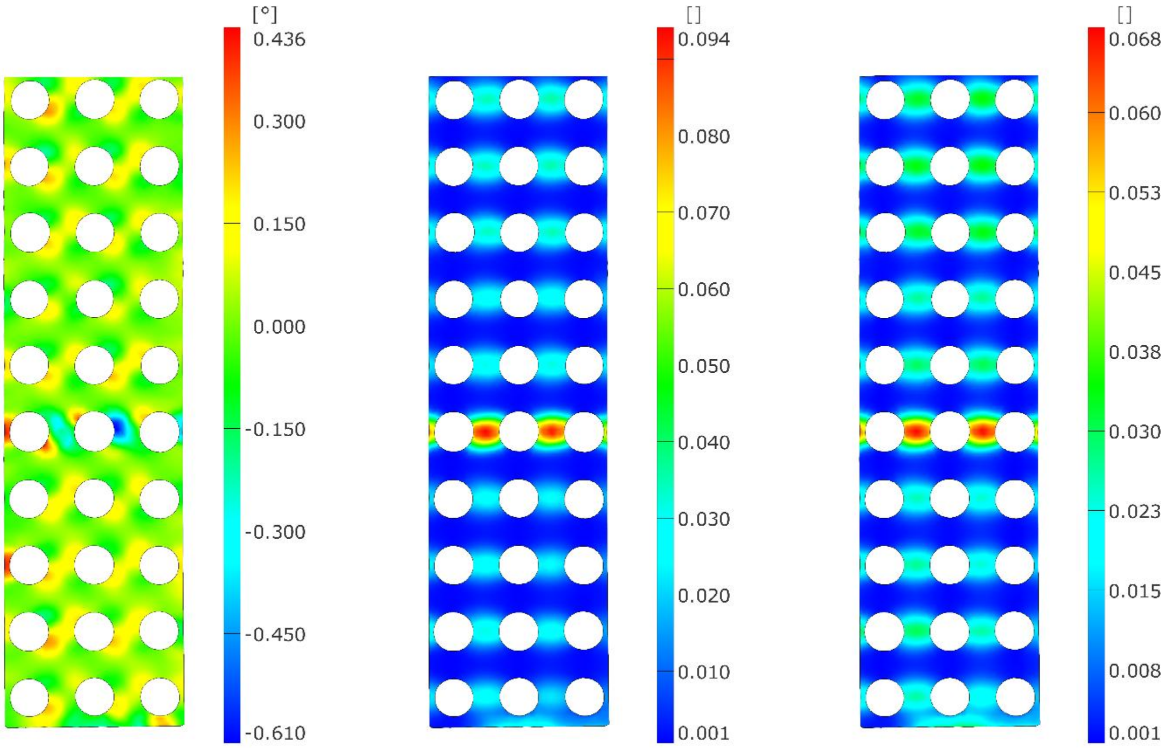

(d) (e) (f)

Figure 4: The maps of specific strains immediately before the occurrence of fracture for case C9: (a) – Major strain [mm/mm]; (b) – Minor strain [mm/mm]; (c) – Thickness reduction [mm/mm]; (d) – Shear angle [°]; (e) – Von Mises equivalent strain [mm/mm] and (f) – Tresca equivalent strain [mm/mm]

Figure 4,a present the results of the major strain expressed in mm/mm, with values ranging from approximately 0.000 to 0.084 mm/mm for case C9. For most of the specimen area, the strain remains relatively low and uniformly distributed, indicating stable deformation away from critical regions. However, the presence of perforations leads to a markedly heterogeneous strain field due to local reductions in the effective area.

Strain localization is observed primarily within the ligaments between adjacent perforations oriented transverse to the loading direction. These regions exhibit horizontal bands of elevated major strain, reflecting preferential plastic flow paths imposed by the specimen geometry. The strongest localization occurs near the mid-height of the gauge section, where the major strain reaches its maximum values, exceeding 0.070 mm/mm and approaching 0.084 mm/mm for case C9. This highly localized strain band is confined to a narrow ligament between perforations and represents the dominant deformation mechanism at the final stage of loading. No comparable strain levels are detected elsewhere in the specimen, confirming that impending fracture is governed by localized geometric constraints rather than global necking.

The minor strain values (Figure 4, b) are predominantly negative throughout the specimen area, with magnitudes ranging approximately from −0.011 mm/mm to values close to zero. This strain state reflects transverse contraction associated with Poisson's effect under uniaxial tensile loading. Over large areas of the specimen, the minor strain remains relatively uniform, indicating stable lateral deformation away from regions affected by geometric discontinuities. Localized bands of increased negative minor strain develop within the ligaments connecting adjacent holes, particularly along horizontal directions transverse to the applied load. These bands corresponding to minor strain values reaching −0.008 to −0.011 mm/mm for case C9.

The strongest localization of the minor strain occurs near the central portion of the gauge length, coinciding with the region where the major strain exhibits pronounced localization immediately prior to fracture. In this zone, the minor strain becomes highly concentrated within a narrow ligament between perforations, indicating enhanced transverse contraction driven by severe plastic flow and geometric constraint. The coexistence of high positive major strain and strongly localized negative minor strain in this region suggests the development of a highly non-uniform, multiaxial strain state. In contrast, regions away from the critical ligament exhibit smoother minor strain gradients and lower absolute values, confirming that the deformation leading to fracture is governed by localized instability rather than global lateral contraction.

The thickness reduction (Figure 4, c) shows the same variation as the major strain, with values concentrated at the location where the fracture will occur. The thickness reduction values ranging from approximately -0.001 to 0.078 mm/mm for case C9.

The shear angle (Figure 4, d) corresponds also to the deformation state immediately prior to fracture and is expressed in degrees. Over most of the gauge section, the shear angle remains close to zero. This behaviour reflects the nominal uniaxial loading condition and the global symmetry of the specimen, which limit large-scale shear deformation away from local geometric discontinuities. Localized shear angle variations are observed in the vicinity of the circular perforations, where the stress state deviates from pure uniaxial tension due to geometric constraint. Alternating regions of positive and negative shear strain develop around the hole edges, forming characteristic local patterns associated with non-uniform displacement gradients.

The most significant shear strain localization is observed near the central region of the gauge length, coinciding with the ligament where pronounced major and minor strain localization occurs immediately prior to fracture. In this region, the shear strain reaches peak magnitudes of approximately +0.44° and −0.61° for case C9. This strongly localized shear angle band exhibits a slight inclination relative to the transverse direction, suggesting rotation of the principal strain axes and the development of a complex multiaxial deformation state. The coexistence of high shear angle with elevated major strain and localized transverse contraction indicates severe plastic flow accompanied by material rotation in the critical ligament.

Outside this localized zone, the shear angle gradients are relatively mild and symmetrically distributed, indicating that shear deformation plays a secondary role in the overall structural response until the onset of localization.

Also, the von Mises strain and Tresca strain values have the same type of variation with major strain. These vary between 0.001 and 0.094 mm/mm (Von Mises strain) and 0.001 and 0.0068 mm/mm (Tresca strain) respectively for case C9.

Table 3 presents the average values for the local major strain ε_1 (mm/mm), local minor strain ε_2 (mm/mm), local thickness reduction ε_3 (mm/mm), and local von Mises strain ε_{VM} (mm/mm).

Table 3: The local results of the digital image corelation (mean values)

Codification	Diameter [mm]	Distance [mm]	Major strain ε_1 [mm/mm]	Minor strain ε_2 [mm/mm]	Thickness reduction ε_3 [mm/mm]	Von Mises strain ε_{VM} [mm/mm]
C1	2.5	2	0.047	-0.030	0.045	0.056
C2	2.5	3	0.051	-0.024	0.049	0.061
C3	2.5	4	0.055	-0.019	0.054	0.067
C4	3	2	0.053	-0.026	0.051	0.063
C5	3	3	0.059	-0.019	0.055	0.071
C6	3	4	0.073	-0.014	0.059	0.080
C7	4	2	0.062	-0.018	0.060	0.082
C8	4	3	0.067	-0.015	0.064	0.088
C9	4	4	0.084	-0.012	0.079	0.095

The combined digital image corelation results demonstrate that fracture initiation in the perforated aluminium EN AW 5754 H22 alloy specimen is governed by a highly localized, multiaxial deformation state characterized by intense shear, tensile stretching, and transverse contraction.

4. CONCLUSIONS

Following the uniaxial tensile test of perforated sheets, the variations graphs of the parameters of interest depending on the perforation diameter and the distance between two adjacent perforations were plotted in Matlab (Figure 5).

DOI: 10.2478/aucts-2025-0001
ACTA UNIVERSITATIS CIBINIENSIS – TECHNICAL SERIES
Vol. 77 2025

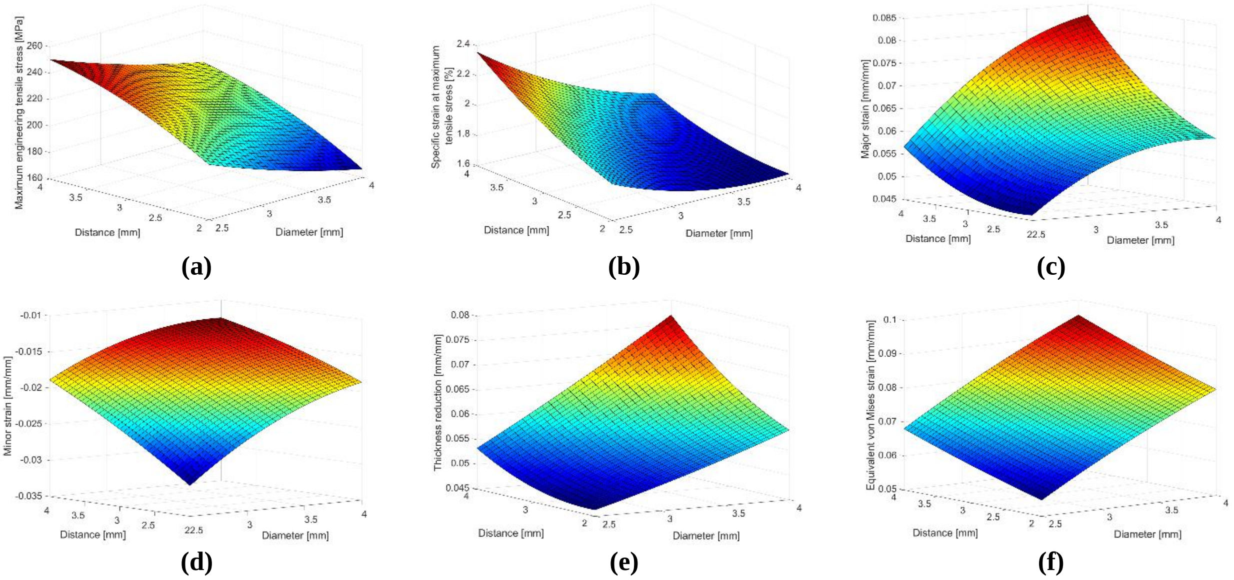

Figure 5: The surface plot for the main results: (a) – Maximum engineering stress [MPa]; (b) – Specific strain corresponding maximum tensile stress [%]; (c) – Local major strain [mm/mm]; (d) – Local minor strain [mm/mm]; (e) – Local thickness reduction [mm/mm]; (e) – Local Von Mises equivalent strain [mm/mm]

Based on the results contained in Tables 2 and 3 and the graphs presented in Figure 5, the following conclusions can be drawn:

- maximum tensile stress and the corresponding strain increase with increasing distance between two perforations and decrease with increasing perforation diameter.
- major strain, thickness reduction, and von Mises strain increase with both increasing distance between two perforations and perforation diameter, whereas the compressive minor strain decreases in magnitude.
- increasing distance between two perforations reduces stress concentration and/or constraint effects, allowing the material to sustain higher tensile stress before fracture occurs.
- larger perforation diameters lead to lower maximum tensile stress, likely due to increased load distribution, reduced local stress intensity, or geometric stiffening.
- increasing distance between two perforations allows greater in-plane deformation before localization, indicating reduced geometric constraint and enhanced strain accumulation.
- increasing distance between two perforations reduces geometric constraint and promotes strain localization, leading to higher equivalent plastic strain.
- larger perforations diameters further enhance overall deformability by enabling a more uniform strain distribution and increased through-thickness thinning.

5. REFERENCES

1. You, H., Zhang, L., Lin, X., Tang, P., Du, Q., Stress concentration characteristics and coefficient modification for DC04 steel with holes of finite thickness. *Frontiers in Materials*, 12, Article 1692324, (2025).
2. Lavrentev, S. Y., Mokryakov, V. V., Chentsov, A. V., Effective elastic moduli of perforated plates containing a rectangular lattice of circular holes. *Mechanics of Solids*, 56(3), pp. 296-300, (2021).
3. Mengsha, S., Chunyu, Z., Yuheng, C., Wang, W., Experimental and theoretical evaluation of influence of hole size on deformation and fracture of elastic perforated plate. *Mechanics of Materials*, 187, Article 104841 (2023).
4. Tang, H., Wen, T., Zhou, Y., You, J., Ma, D., Study on the wrinkling behavior of perforated metallic plates using uniaxial tensile tests. *Thin-Walled Structures*, 167, Article 108132, (2021).
5. Wang, F., Yan, R., Li, M., Sun, J., Study on Ultimate Tensile Strength of Carbon/Glass Hybrid Composite Perforated Plate. *Wuhan Ligong Daxue Xuebao (Jiaotong Kexue Yu Gongcheng Ban)/Journal of Wuhan University of Technology (Transportation Science and Engineering)*, 48(5), pp. 923-928

DOI: 10.2478/aucts-2025-0001

(2024).
6. Hu, B., Chen, X., Deng, F., Sun, X., Evaluation of failure criteria for residual tensile strength of composite laminates with circular holes. *Vibroengineering Procedia*, vol. 49, pp. 212-219, (2023).
7. Jing, L., Peng, S., Li, X., Li, S., Yan, Y., Jing, W., Uniaxial failure test and simulation of plate with circular hole containing single crack. *China Mining Magazine*, 31(7), pp. 174-182 (2022).
8. Scherer, J. M., Brach, S., Bleyer, J., An assessment of anisotropic phase-field models of brittle fracture. *Computer Methods in Applied Mechanics and Engineering*, 395, Article 115036 (2022).
9. Kinoshita, K., Suzuki, Y., Kumagai, T., Watanabe, O., Matsuda, A., Multiple crack extension and temperature effect of perforated plate in elevated temperature fatigue test. in American Society of Mechanical Engineers, *ASME 2013 Pressure Vessels and Piping Conference*, vol. 6 A, Article number: PVP2013-97871 (2013).
10. Chen, B., Wang, Y., Ye, J., Lim, J. B. P., & Hai, L., Shear resistance of perforated QN1803 high-strength stainless steel plate girders through experimental testing and numerical analysis. *Thin-Walled Structures*, 196, Article 111505 (2024).
11. Saad-Eldeen, S., Garbatov, Y., Experimental and Numerical Analysis of Structural Capacity of Perforated Stiffened Plates. *Journal of Marine Science and Engineering*, *11*(4), Article 842, (2023).
12. Huang, B. T., Dai, J. G., Weng, K. F., Zhu, J. X., Shah, S. P., Flexural Performance of UHPC-Concrete-ECC Composite Member Reinforced with Perforated Steel Plates. *Journal of Structural Engineering*, 147(6), Article 04021065 (2021).
13. Granum, H., Aune, V., Borvik, T., Hopperstad, O. S., Aluminium plates with pre-formed slits subjected to blast loading. *EPJ Web of Conferences*, vol. 183, Article Number 01032, (2018).
14. Munemoto, S., Sonoda, Y., An analytical study on the dynamic strength of perforated steel plate shear connectors. *10th International Conference on Shock and Impact Loads on Structures* - Singapore, Singapore, pp. 433-440, (2013).
15. Leminen, V., Tanninen, P., Pesonen, A., Varis, J., Effect of mechanical perforation on the press-forming process of paperboard. *Procedia Manufacturing*, vol. 38, pp. 1402-1408, (2019).
16. Lecompte, D., Smits, A., Sol, H., Vantomme, J., van Hemelrijck, D., Mixed numerical-experimental technique for orthotropic parameter identification using biaxial tensile tests on cruciform specimens. *International Journal of Solids and Structures*, 44(5), pp. 1643-1656 (2007).